

Article

A Versatile Unitary Transformation Framework for an Optimal Bath Construction in Density-Matrix Based Quantum Embedding Approaches

Quentin Marécat *  and Matthieu Saubanère 

ICGM, Université de Montpellier, CNRS, ENSCM, 34000 Montpellier, France; matthieu.saubanere@cnrs.fr

* Correspondence: quentin.marecat@umontpellier.fr

Abstract: The performance of embedding methods is directly tied to the quality of the bath orbital construction. In this paper, we develop a versatile framework, enabling the investigation of the optimal construction of the orbitals of the bath. As of today, in state-of-the-art embedding methods, the orbitals of the bath are constructed by performing a Singular Value Decomposition (SVD) on the impurity-environment part of the one-body reduced density matrix, as originally presented in Density Matrix Embedding Theory. Recently, the equivalence between the SVD protocol and the use of unitary transformation, the so-called Block-Householder transformation, has been established. We present a generalization of the Block-Householder transformation by introducing additional flexible parameters. The additional parameters are optimized such that the bath-orbitals fulfill physically motivated constraints. The efficiency of the approach is discussed and exemplified in the context of the half-filled Hubbard model in one-dimension.

Keywords: one-body reduced density matrix functional embedding; effective Hamiltonian; Hubbard model; unitary transformation; divide-and-conquer algorithm; density matrix embedding theory



Citation: Marécat, Q.; Saubanère, M. A Versatile Unitary Transformation Framework for an Optimal Bath Construction in Density-Matrix Based Quantum Embedding Approaches. *Computation* **2023**, *11*, 203. <https://doi.org/10.3390/computation11100203>

Academic Editors: Karlheinz Schwarz and Henry Chermette

Received: 26 July 2023

Revised: 6 October 2023

Accepted: 10 October 2023

Published: 11 October 2023



Copyright: © 2023 by the authors. Licensee MDPI, Basel, Switzerland. This article is an open access article distributed under the terms and conditions of the Creative Commons Attribution (CC BY) license (<https://creativecommons.org/licenses/by/4.0/>).

1. Introduction

Quantum chemistry relies on solving the Schrödinger equation, but this quickly becomes computationally prohibitive for practical systems due to the exponential increase in numerical cost as the system size grows. Numerically exact solutions are challenging to obtain for systems containing around 15 to 20 electrons. In this context, quantum embedding methods [1,2] have emerged as a powerful tool, particularly for the study of strongly correlated systems [3–5], where traditional methods often fall short [6,7]. In short, an embedding protocol consists of partitioning the original extended system containing a large number of N orbitals into fragments. Each fragment, often referred to as an *impurity*, is complemented with bath orbitals to define an effective reduced system described by an effective Hamiltonian. The reduced system, comprising the fragment and bath (denoted as the *cluster*), contains N_f orbitals of the fragment, which interact with the additional N_b bath orbitals. Ideally, the fragment and bath reduced system is entirely decoupled from the rest of the system containing N_e orbitals, referred to as the *environment* of the cluster. The cornerstone of these embedding methods is the construction of bath orbitals associated with a fragment in order to derive the effective Hamiltonian of the reduced system. This effective Hamiltonian captures the physics of the larger original environment while integrating out most of its degrees of freedom. Consequently, it provides a highly efficient approach to treat localized electron correlation without the need to explicitly consider the entire system, thus balancing computational feasibility with accuracy. Different embedding strategies have been proposed in the literature to construct such a reduced effective Hamiltonian.

Among these embedding strategies, some rely on the Green's function formalism, which focuses on single-particle excitations and can naturally incorporate electronic correlation effects. In particular, within the dynamical mean-field theory (DMFT) formal-

ism [8–10], the effective Hamiltonian is an effective Anderson impurity model (AIM) [11], and is derived self-consistently using the Green’s function of the system. Note that various alternative embedding approaches using the Green’s function have been developed to derive effective AIM [12–14] or other effective Hamiltonians [15,16].

In parallel, embedding approaches have been proposed within the one-body Reduced Density-Matrix (1RDM) formalism. The aim is to design a protocol to construct the bath orbitals, and the corresponding effective Hamiltonian of the cluster, that become functional of the 1RDM. Among the different approaches recently proposed [17–20], the pioneering work of Knizia et al. [21] proposes to define the effective Hamiltonians by means of the Schmidt decomposition of a single Slater determinant $|\Phi\rangle$ that is univocally associated with an idempotent 1RDM γ^0 with the Density Matrix Embedding Theory (DMET). The Schmidt decomposition of $|\Phi\rangle$ defines a projector via a Singular Value Decomposition (SVD) of the fragment-environment part of γ^0 [22–24]. Indeed, SVD is known to yield the most compact representation of all information contained within the fragment-environment 1RDM. This approach imposes that the bath constructed through the SVD contains as many orbitals as the impurity fragment, and also that only idempotent 1RDM can be used to describe the extended system. Over the past decade, different variations and improvements of the original DMET have been investigated and benchmarked [25–29]. Recently, Sekaran et al. [23,30] proposed to use a specific unitary transformation, defined as a functional of the 1RDM, to construct the bath orbitals [30]. The aforementioned unitary transformation is known as the Block-Householder transformation (BHT). They demonstrated that the SVD of the fragment-environment 1RDM is equivalent to the BHT, even for a non-idempotent 1RDM [24]. Despite the appealing compactness of the resulting sub-space of the bath, it should be noted that there is no inherent physical reason to believe that such decomposition yields the “best” effective Hamiltonian for reproducing the interactions between the fragment and its environment.

In this paper, our contributions lie in the proposal of a versatile framework that generalizes the Block-Householder transformation, introduction of additional degrees of freedom for the construction of bath orbitals, and derivation of the effective Hamiltonian. As a result, additional constraints are required for the bath orbitals such as maximally disentangling the cluster from the environment, or matching density matrices. The effects of the additional constraints to optimally construct the orbitals of the bath are benchmarked on the well-known but non-trivial half-band filled one-dimensional Hubbard model [31], following the divide-and-conquer (DaC) algorithm proposed in a previous work by the authors [32].

2. Theory

In this section, we recall the DaC algorithm proposed in Ref. [32], represented in Figure 1, applied to the paramagnetic Hubbard ring. The Hubbard Hamiltonian is given by

$$\hat{H} = -t \sum_{\langle ij \rangle \sigma} \hat{c}_{i\sigma}^\dagger \hat{c}_{j\sigma} + U \sum_i \hat{n}_{i\uparrow} \hat{n}_{i\downarrow} \quad (1)$$

where $\hat{c}_{i\sigma}^\dagger$ ($\hat{c}_{i\sigma}$) corresponds to the creation (annihilation) of an electron of spin σ on the i -th orthogonal atomic (or localized) orbital, $\hat{n}_{i\sigma}$ is the counting operator equal to $\hat{c}_{i\sigma}^\dagger \hat{c}_{i\sigma}$. Indexes $\langle ij \rangle$ refer at nearest neighbor orbitals. $-t$ corresponds to the hopping integral, while U stands for the Coulomb integral.

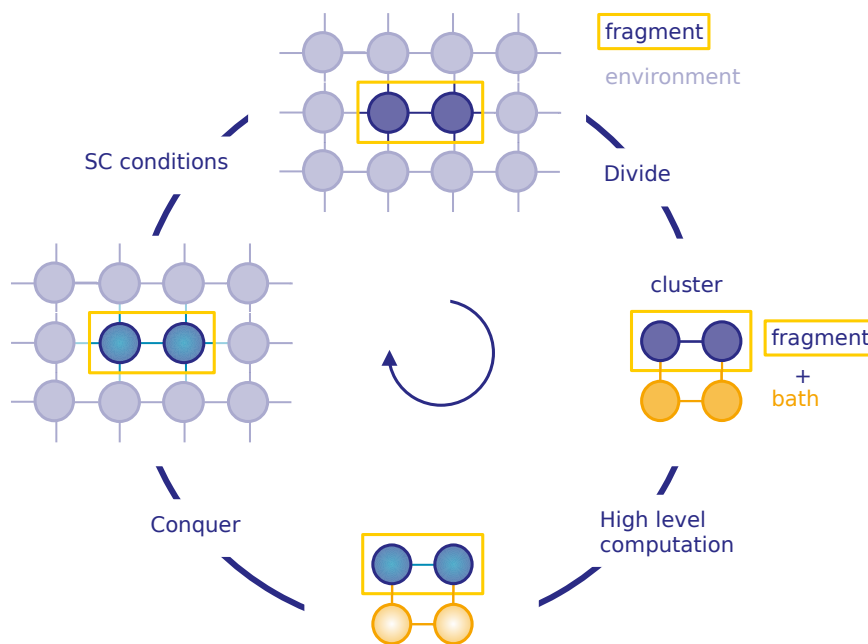


Figure 1. Schematic Representation of the DaC Algorithm for Two Impurity Orbitals in the Fragment.

2.1. Quantum Bath from the Block-Householder Transformation

In this section, we recall the generic construction of the unitary Block-Householder matrix \mathbf{R}^σ , following the work of Sekaran et al. [30]. The unitary transformation \mathbf{R}^σ is defined as a functional of the spin 1RDM γ^σ . It performs the rotation of the mono-electronic basis set as

$$\tilde{c}_{i\sigma}^\dagger = \sum_k \mathbf{R}_{ik}^{\sigma\dagger} c_{k\sigma}^\dagger, \quad \tilde{c}_{i\sigma} = \sum_k \mathbf{R}_{ik}^\sigma c_{k\sigma}, \tag{2}$$

where $\tilde{c}_{i\sigma}^\dagger$ ($\tilde{c}_{i\sigma}$) stands for the creation (annihilation) operators of an electron in the i -th orbital with spin σ expressed in the \mathbf{R}^σ representation, respectively. The latter is denoted by a $\tilde{\cdot}$ in the following. It follows that the system is divided into a compact subset of $N_i + N_b$ orbitals, the cluster, interacting minimally with a large number of N_e orbitals. More precisely, the unitary transformation is designed such that (i) the fragment in the full system is the same as in the cluster

$$\tilde{c}_{i\sigma}^\dagger = c_{i\sigma}^\dagger, \quad \tilde{c}_{i\sigma} = c_{i\sigma} \quad \forall i \in \text{fragment}, \tag{3}$$

or equivalently $\mathbf{R}^\sigma = \delta_{ik}$ where i belongs to the fragment, and (ii) the fragment is fully disconnected from the environment at the one-body level,

$$\tilde{\gamma}_{ie}^\sigma = \sum_k \mathbf{R}_{ek}^\sigma \gamma_{ik}^\sigma = 0 \quad \forall i \in \text{fragment}, \forall e \in \text{environment}. \tag{4}$$

Numerous unitary transformations satisfy Conditions (3) and (4) resulting in identical bath orbitals subspace [33,34]. Among all these transformations, we focus explicitly on the unitary Block-Householder matrix \mathbf{R}^σ defined using an auxiliary matrix $\mathbf{V}[\gamma^\sigma] \in \mathbb{R}_{NN_i}$, with

$$\mathbf{R}^\sigma = \mathbf{I} - 2\mathbf{V}(\mathbf{V}^T\mathbf{V})^{-1}\mathbf{V}^T, \tag{5}$$

where \mathbf{I} stands for the identity matrix. By construction, \mathbf{R}^σ is a normal involution (i.e., $\mathbf{R}^{\sigma^{-1}} = \mathbf{R}^\sigma$, $\mathbf{R}^{\sigma^T} = \mathbf{R}^\sigma$ and $\det(\mathbf{R}^\sigma) = (-1)^{N_i}$) with eigenvalues $\{1, -1\}$, and

$\dim(\text{Ker}(\mathbf{R}^\sigma + \mathbf{I})) = r = N_i$. The matrix \mathbf{V} is given as follows.

$$\mathbf{V} = \begin{pmatrix} \mathbf{0}_{:N_i}^r \\ \gamma_{N_i:2N_i}^r + \mathbf{X}_{:N_i}^r \\ \gamma_{2N_i:N}^r \end{pmatrix}. \tag{6}$$

The notation $\mathbf{A}_{i:j}^c$ corresponds to a "pythonic" notation where only the elements from i -th to the j -th lines for first c -th columns of the matrix \mathbf{A} . For example, the square matrix $\gamma_{N_i:2N_i}^r$ refers to the first $r = N_i$ -th columns of γ^σ from the N_i -th element to the $2N_i$ -th. The null matrix $\mathbf{0}_{:N_i}^r$ allows to fix the identity in Equation (3) on the subspace corresponding to the fragment, and $\mathbf{X}_{:N_i}^r$ is a square matrix to be determined in order to satisfy Condition (4). To this aim, Rotella et al. [35] proposed a systematic construction with

$$\mathbf{X}_{:N_i}^r = \mathbf{P}^T \sqrt{\mathbf{D}} \mathbf{P} \gamma_{N_i:2N_i}^r, \tag{7}$$

and $\sqrt{\mathbf{D}} = \text{diag}_{i=1}^N \{ \sqrt{d_i} \}$, where the non-negative scalar d_i and the orthogonal matrix \mathbf{P} are defined by

$$\mathbf{I} + \left(\gamma_{2N_i:N}^r \gamma_{N_i:2N_i}^{r-1} \right)^T \left(\gamma_{2N_i:N}^r \gamma_{N_i:2N_i}^{r-1} \right) = \mathbf{P}^T \mathbf{D} \mathbf{P}, \tag{8}$$

and \mathbf{D} (\mathbf{P}) is eigenvalues (eigenvectors) matrix of the left-sided matrix in Equation (8), respectively. The construction of $\mathbf{X}_{:N_i}^r$ in Equation (7) holds only if the square matrix $\gamma_{N_i:2N_i}^r$ is invertible. Then we obtain

$$(\mathbf{R}^\sigma \gamma^\sigma)^r = \begin{pmatrix} \gamma_{:N_i}^r \\ -\mathbf{X}_{:N_i}^r \\ \mathbf{0}_{:N_e}^r \end{pmatrix}. \tag{9}$$

Equation (9) is strictly equivalent as the conditions defined in Equations (3) and (4), i.e., the transformation preserves the orbitals of the fragment in the cluster and disconnects the fragment from the environment at the one-body level.

A recent study expounded on the mathematical equivalence between the bath orbitals constructed using the BHt of the 1RDM and the SVD of the fragment-environment 1RDM [24]. As a result of this equivalence, the BHt provides the most compact representation, encapsulating information pertaining to the one-body level interactions between the fragment and its environment. Once the BHt has been presented to construct the orbitals of the bath, we briefly recall the procedure based on \mathbf{R}^σ in order to define an effective, yet approximated, embedded Hamiltonian. Details and discussion on the straightforward generalization to the ab initio Hamiltonian can be found in Ref. [32]. Following Equation (2), we perform the BHt of the full Hamiltonian (1) to derive the Hamiltonian \tilde{H} ,

$$\tilde{H} = \sum_{ij\sigma} \tilde{t}_{ij} \tilde{c}_{i\sigma}^\dagger \tilde{c}_{j\sigma} + \sum_{ijkl} \tilde{U}_{ijkl} \tilde{c}_{i\uparrow}^\dagger \tilde{c}_{j\uparrow}^\dagger \tilde{c}_{k\downarrow} \tilde{c}_{l\downarrow}, \tag{10}$$

where single- and two-body integrals in the \mathbf{R}^σ -representation \tilde{t}_{ij} and \tilde{U}_{ijkl} , respectively, are calculated in the same manner,

$$\tilde{t}_{ij} = - \sum_{kl} t_{kl} \mathbf{R}_{ik}^{\sigma\dagger} \mathbf{R}_{jl}^\sigma, \tag{11}$$

$$\tilde{U}_{ijkl} = U \sum_m \mathbf{R}_{im}^{\sigma\dagger} \mathbf{R}_{jm}^\sigma \mathbf{R}_{km}^{\bar{\sigma}\dagger} \mathbf{R}_{lm}^{\bar{\sigma}}. \tag{12}$$

At this point, the complexity of solving Hamiltonian (10) is the same as the original Hamiltonian (1). Considering that the BHt maximally uncouples the fragment from the environment through the orbitals of the bath, an approximation for the effective Hamiltonian on the cluster \tilde{H}^c is obtained by projecting the Hamiltonian (10) onto the cluster

orbitals thus drastically reduce the numerical complexity of the system by solving a system of $N_i + N_b \ll N$ orbitals. Part of the cluster-environment two-body interactions are taken into account at a mean-field level in \bar{H}_{MF}^{ce} with

$$\bar{H}_{MF}^{ce}[\gamma^\sigma] = \sum_{\sigma} \sum_{i,j \in \text{cluster}} \tilde{c}_{i\sigma}^\dagger \tilde{c}_{j\sigma} \sum_{(kl)} \tilde{U}_{ijkl} \sum_{mn} \mathbf{R}_{km}^{\sigma\dagger} \mathbf{R}_{nl}^{\sigma} \gamma_{kl}^{\bar{\sigma}} + \text{h.c.}, \tag{13}$$

where the notation (kl) refers to pairs of orbitals in \mathbf{R}^σ -representation such that at least k or l belongs to the environment. Finally, an effective homogeneous chemical potential μ_{emb} is added within the bath to preserve the total number of electrons in the fragment. All together, the cluster effective Hamiltonian for which the ground-state solution is numerically obtained, reads

$$\bar{H}_{\text{eff}}^c = \bar{H}^c + \bar{H}_{MF}^{ce} + \mu_{\text{emb}} \sum_{i \in \text{bath}} \tilde{c}_i^\dagger \tilde{c}_i. \tag{14}$$

Likely influenced by the non-interacting character of the bath in DMFT, the non-local interaction integrals \tilde{U}_{ijkl} that naturally arise in the bath have been initially neglected in DMET, leading to a Anderson impurity model in the cluster [21]. This approximation is called non-interacting bath (NIB) in contrast to the interacting bath (IB) version of DMET where \tilde{U}_{ijkl} are explicitly taken into account [22]. The similar distinction between NIB and IB can also be considered using the BHt to construct the orbitals of the bath [30,32].

Interestingly for non-interacting Hamiltonian ($U = 0$), for which the associated 1RDM is idempotent ($\gamma^{\sigma^2} = \gamma^\sigma$), the BHT of the 1RDM leads to a perfect decoupling of 1RDMs of the clusters (Equation (4) being fulfilled $\forall i \in$ the cluster instead of the fragment). It corresponds to an exact factorization of the underlying associated wave-function $|\Psi\rangle = |\phi\rangle$, where $|\phi\rangle$ refers to a single Slater determinant. The factorization of the wave-function gives

$$\mathbf{R}|\phi\rangle = \hat{A}|\tilde{\phi}^c\rangle|\tilde{\phi}^e\rangle, \tag{15}$$

where $|\tilde{\phi}^c\rangle$ ($|\tilde{\phi}^e\rangle$) is an anti-symmetrized product of orbitals that belong solely to the cluster (environment). $\mathbf{R}|\phi\rangle$ is a shortcut notation, such that the Slater determinant is expressed in the \mathbf{R}^σ -representation using the Equation (2). Consequently, in this specific case, the projected cluster Hamiltonian proposed in Equation (14) serves as a useful approximation and is solved to extract exact local properties of the impurity site, where the ground-state wave function $|\tilde{\phi}\rangle$ is equal to $|\tilde{\phi}^c\rangle$ [30].

The Hamiltonian (14) is de facto a functional of the 1RDM via the definition of $\mathbf{R}^\sigma[\gamma^\sigma]$. Several studies have developed self-consistent schemes predicated on the local cluster 1RDM calculated with Equation (14), as seen in DMET [21] and more recent DaC algorithms [32]. Regardless of the self-consistent matching or conquer strategy employed, the efficiency of the method hinges crucially on the ability of the effective cluster Hamiltonian (14) to locally mimic the full Hamiltonian on the fragment. On this subject, there is no unambiguously definitive approach to determine what exactly constitutes “mimicry”. To address this challenge, we propose in the following sections to generalize Equation (6), introducing variational parameters to explore different flavours of embedding.

2.2. Quantum Bath from a Versatile Unitary Transformation Framework

Following the philosophy of exact diagonalization solver in DMFT [36], we would like to control the number of bath orbitals, independently of the number of impurity orbitals in the fragment, in order to systematically gain a better description of the interactions of the fragment with the environment. As shown schematically in Figure 2, the BHt leaves the fragment (dark blue square) unchanged in the cluster (gray square), and interacts solely with the bath (orange square), where the number of bath orbitals is the same as in the fragment. In the following, we give a general and flexible definition of the unitary matrix $\mathbf{R}^\sigma[\gamma^\sigma]$ to obtain an optimized cluster, composed of N_i impurities coupled to $N_b \geq N_i$ bath orbitals.

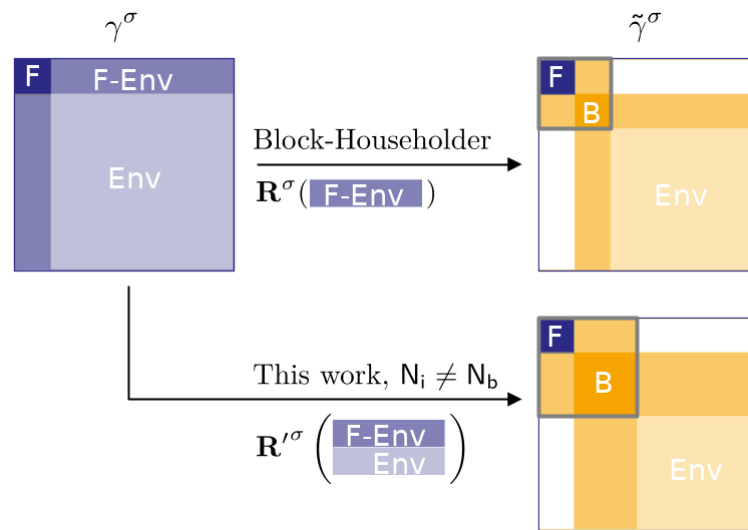


Figure 2. Schematic representation of the BHt and the generalization, both functionals of the 1RDM. Small dark blue squares correspond to the fragment 1RDM in the system, identical as in the cluster, and orange squares correspond to bath 1RDM in the cluster. The gray squares correspond to the cluster.

In what follows, spin index σ is omitted for clarity. Similarly as the BHt, we use the auxiliary matrix \mathbf{V}' with

$$\mathbf{R}'^\sigma = \mathbf{I} - 2\mathbf{V}'(\mathbf{V}'^T \mathbf{V}')^{-1} \mathbf{V}'^T. \tag{16}$$

The auxiliary matrix $\mathbf{V}' \in \mathbb{R}_{Nr}$, where $N_i \leq r \leq N$ refers to the rank of the auxiliary matrix, is constructed as following

$$\mathbf{V}' = \begin{pmatrix} \mathbf{0}_{:N_i}^r \\ \gamma_{N_i:N_i+N_b}^r - \mathbf{X}'_{:N_b}{}^r \\ \gamma_{N_i+N_b:N}^r \end{pmatrix}, \tag{17}$$

and indexes N_i, N_b, N_e refer to the number of impurity orbitals in the fragment, the number of bath orbitals and the number of orbitals in the environment, respectively. $\gamma_{N_i:N_i+N_b}^r$ ($\gamma_{N_i+N_b:N}^r$) corresponds to the r first columns of the spin 1RDM γ^σ and the N_b lines (N_e) after the N_i -th ($N_i + N_b$ -th) first one. At this point, condition (3) (preservation of the fragment in the cluster) is already satisfied. The matrix $\mathbf{X}'_{:N_b}{}^r$ must be determined in order to preserve condition (4), i.e., it must satisfy the following equation,

$$(\mathbf{X}'_{:N_b}{}^r - \gamma_{N_i:N_i+N_b}^r)^T (\mathbf{X}'_{:N_b}{}^{N_i} + \gamma_{N_i:N_i+N_b}^{N_i}) = \gamma_{N_i+N_b:N}^{rT} \gamma_{N_i+N_b:N}^{N_i}. \tag{18}$$

In the Equation (18), we distinguish the matrix $\mathbf{X}'_{:N_b}{}^r$ from the matrix $\mathbf{X}'_{:N_b}{}^{N_i}$. The latter contains only the first N_i -th column(s) of $\mathbf{X}'_{:N_b}{}^r$. More precisely, the matrix $\mathbf{X}'_{:N_b}{}^r$ is build from the concatenation of matrices $\mathbf{X}'_{:N_b}{}^{N_i}$ and $\mathbf{X}'_{:N_b}{}^{N_i:r}$. In practice, the nonlinear Equation (18) can be solved numerically. In the following, we discuss only the single impurity case $N_i = 1$, where Equation (18) is solved analytically. In this simple case, the matrix $\mathbf{X}'_{:N_b}{}^{N_i} = \mathbf{X}'_{:N_b}{}^1$ is reduced to a vector. In the same manner, we split the matrix $\mathbf{X}'_{:N_b}{}^{N_i:r}$ into a complete set of vector, denoted as $\mathbf{X}'_{:N_b}{}^j$ where $1 < j \leq r$. For the single impurity case, the Equation (18)

becomes

$$(\mathbf{X}'_{:N_b}{}^1 - \gamma_{N_i:N_i+N_b}^1)^T (\mathbf{X}'_{:N_b}{}^1 + \gamma_{N_i:N_i+N_b}^1) = \gamma_{N_i+N_b:N}^1 \gamma_{N_i+N_b:N}^1 \tag{19}$$

$$(\mathbf{X}'_{:N_b}{}^j - \gamma_{N_i:N_i+N_b}^j)^T (\mathbf{X}'_{:N_b}{}^j + \gamma_{N_i:N_i+N_b}^j) = \gamma_{N_i+N_b:N}^j \gamma_{N_i+N_b:N}^j \quad \forall 1 < j \leq r. \tag{20}$$

The Equation (19) is nonlinear and constrains the norm of the vector $\mathbf{X}'_{:N_b}{}^1$. More precisely, this equation is fulfilled for any vectors $\mathbf{X}'_{:N_b}{}^1$ satisfying

$$\|\mathbf{X}'_{:N_b}{}^1\| = \|\gamma_{N_i:N_i+N_b}^1\| + \|\gamma_{N_i+N_b:N}^1\|, \tag{21}$$

where $\|\mathbf{v}\| = \mathbf{v}^T \mathbf{v}$ refers to the norm of the vector \mathbf{v} . The Equation (20) exists only for $r > N_i$ and is linear for $\mathbf{X}'_{:N_b}{}^j$, corresponding to a scalar-product preservation, and can be written for all $1 < j \leq r$ as follows,

$$\mathbf{X}'_{:N_b}{}^{jT} (\mathbf{X}'_{:N_b}{}^1 + \gamma_{N_i:N_i+N_b}^1) = \gamma_{N_i:N_i+N_b}^{jT} (\mathbf{X}'_{:N_b}{}^1 + \gamma_{N_i:N_i+N_b}^1) + \gamma_{N_i+N_b:N}^{jT} \gamma_{N_i+N_b:N}^1. \tag{22}$$

We introduce a spherical representation which allows us to express the vectors $\mathbf{X}'_{:N_b}{}^j$ with lengths l^j and a complete set of angles $\{\theta\}$. In this representation, length l^1 (l^j) is used to fulfill norm preservation (21) (scalar product (22)) for $\mathbf{X}'_{:N_b}{}^1$ ($\mathbf{X}'_{:N_b}{}^j$), respectively. The set of angles $\{\theta\}$ are thus completely free and can take any value between $[-\pi, \pi]$. Consequently, we have a complete set of $\{\theta\}$ parameters to construct the corresponding set of different auxiliary matrices defined in Equation (17) satisfying the conditions (3) and (4). The number of free parameters is equal to $r \times (N_b - N_i)$, with $r \geq N_i$. In Figure 3, we illustrate all vectors that can be obtain for $N_i = 1, N_b = 3$ and $r = 2$. Dark blue vectors correspond to the special two impurities $N_i = r = 2$ (or rank two) Block-Householder solution, where the construction of such vectors has been presented in detail in Section 2.1. The rank two BHT preserves the identity over the second impurity, meaning that the axe $N_b = 1$ in the figure corresponds to the second impurity. This transformation is a particular solution of the Equations (21) and (22). Beyond the special BHT, all vectors belonging to the orange sphere are solutions of the Equation (21), such as presented with the orange vector $\mathbf{X}'_{:N_b}{}^1$ for example. The second vector (light blue vector) norm depends on its scalar product with $\mathbf{X}'_{:N_b}{}^1$. Thus, the norm (and the direction) is fixed using Equation (22) and all other angles left are free. More generally, when $r > 1$, every vectors $\mathbf{X}'_{:N_b}{}^j, 1 < j \leq r$ are independent from each other and are correlated to $\mathbf{X}'_{:N_b}{}^1$ solely. With the spherical representation of the vectors $\mathbf{X}'_{:N_b}{}^j$, we have access to a complete set of solutions of the Equations (21) and (22), as a free set of parameters with the angles $\{\theta\}$.

Note that by considering r, N_b and $N'_b > N_b$, the auxiliary matrix $\mathbf{V}'[\mathbf{X}'_{:N_b}{}^r]$ space is not included into $\mathbf{V}'[\mathbf{X}'_{:N'_b}{}^r]$, i.e., any rank r auxiliary matrices expressed using Equation (17) with N_b bath cannot be expressed with an auxiliary matrix with a greater number of bath N'_b . Similarly, if we consider N_b, r and $r' > r$, we get $\mathbf{V}'[\mathbf{X}'_{:N_b}{}^r] \notin \mathbf{V}'[\mathbf{X}'_{:N_b}{}^{r'}]$, which means that different ranks r lead to a specific definition of the cluster.

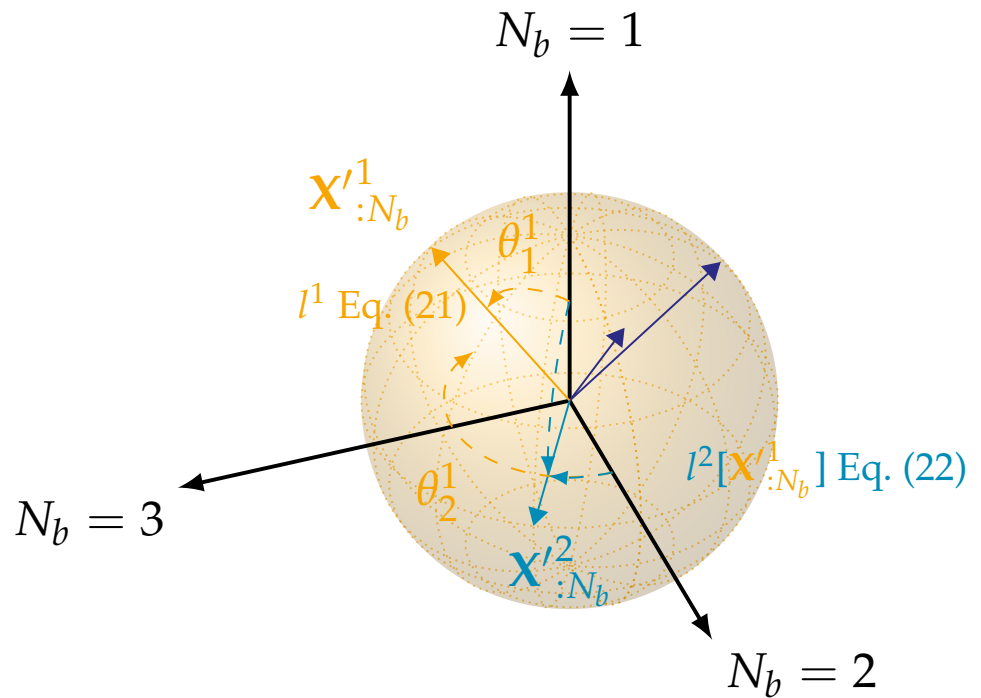


Figure 3. Schematic representation of vectors $\mathbf{X}'^j_{:N_b}$ (orange vector for $j = 1$ and light blue vector for $j = 2$) in spherical representation for the single impurity case $N_i = 1$ and three orbitals in the bath, corresponding to the number of axes. The rank of the transformation is equal to the number of vectors, here with a rank $r = 2$. Dark blue vectors correspond to the two impurities (equivalently $r = 2$) Block-Householder vectors from a 1RDM of a non-interacting 1D-Hubbard system. The length l^1 is fixed according to Equation (21), while lengths $l^j, r \geq j > 1$ depends on the vector $\mathbf{X}'^1_{:N_b}$ following the Equation (22). All angles parameters $\{\theta_i^j\}, 1 \leq i \leq r - N_i$ are free. For example, all vectors belonging to the orange sphere are available as a choice of $\mathbf{X}'^1_{:N_b}$. The number of free parameters is equal to $r \times (N_b - N_i) = 4$ (orange and light blue dashed curves).

At this stage, we have proposed a generic construction of unitary transformations following Equations (16) and (17) that generalize the BHT. Indeed, given an arbitrary number of bath orbitals N_b ($N_b \geq N_i$) and rank r of matrix \mathbf{V}^j ($N_i \leq r \leq N$), we show that we can construct many unitary transformations that fulfill conditions (3) and (4) up to $r \times (N_b - N_i)$ free parameters. In the next section, we propose to use these additional parameters in order to add physically motivated criteria to design bath orbitals.

2.3. Optimization of Free Parameters

The free parameters $\{\theta\}$ are variationally optimized to adjust the bath orbitals using physical insights, unlike the systematic BHT. In what follows, the transformation $\mathbf{R}^{l\sigma}$ is a functional of the spin 1RDM, but also a function of a full set of free parameters $\{\theta\}$ and is denoted as $\mathbf{R}^{l\sigma}[\gamma^\sigma](\{\theta\})$, or in a more compact notation $\mathbf{R}^{l\sigma}(\theta)$. The transformation of γ^σ with the transformation $\mathbf{R}^{l\sigma}(\theta)$ is denoted as $\tilde{\gamma}^\sigma$.

According to the construction of $\mathbf{R}^{l\sigma}(\theta)$ fulfilling constraint (4), the fragment is disconnected from the environment at the one-body level. In the non-interacting case, we show analytically that the Block-Householder ($r = N_i$) disconnects bath orbitals from the environment. However, this is not the case for the correlated 1RDM. Therefore, the set of variational parameters is used to minimize the value of the so-called buffer-zone Δ , which gives a quantitative insight into the disentanglement of the environment cluster at the one

body level and leads to the saddle-point equation

$$\Delta^2(\theta) = \sum_{b \in \text{bath}} \sum_{e \in \text{env}} \tilde{\gamma}_{be}^{\sigma^2}, \tag{23}$$

$$\frac{\partial \Delta(\theta_i)}{\partial \theta_i} = 0 \quad \forall \theta_i \in \{\theta\}. \tag{24}$$

Following a similar philosophy, one could minimize the single-particle Von-Neumann entropy of the truncated 1RDM of the cluster.

From the medium to the strong correlated regime, the buffer-zone Δ is not able to give a quantitative value of the entanglement between the cluster and the environment, where two-body interactions dominate at this regime. In the following, we propose to minimize the square of the Hartree (i.e., mean-field) contribution energy between the cluster and the environment

$$E_{\text{H}}^2(\theta) = \sum_{\sigma, c \in \text{cluster}} \left[\sum_{(jkl)} \left(\tilde{U}(\theta)_{c jkl} \tilde{\gamma}_{c j}^{\sigma} \tilde{\gamma}_{k l}^{\sigma} \right)^2 + \sum_{e \in \text{env}} \left(\tilde{t}_{ce} \tilde{\gamma}_{ce}^{\sigma} \right)^2 \right], \tag{25}$$

$$\frac{\partial E_{\text{H}}^2(\theta_i)}{\partial \theta_i} = 0 \quad \forall \theta_i \in \{\theta\}, \tag{26}$$

where c (e) belongs to the cluster (environment), respectively, and the notation (jkl) refers to pairs of orbitals in $\mathbf{R}^{\prime\sigma}(\theta)$ representation such that at least j , k or l belongs to the environment, and \tilde{t}_{ce} ($\tilde{U}(\theta)_{c jkl}$) defined in Equation (11) (Equation (12)), respectively. In a practical way, the evaluation of E_{H}^2 using Equation (25) is numerically more expensive than the evaluation of Δ .

Finally, inspired by the DMET matching, we propose to design the transformation in order to enforce the matching between density matrix elements connected to the fragment in the transformation space, and in the cluster

$$\min_{\theta} \sum_{ij} \left(\tilde{\gamma}_{ij}^{\sigma} - \tilde{\gamma}_{ij}^{\sigma c} \right)^2 \quad \forall i \in \text{fragment}, \forall j \in \text{cluster}, \tag{27}$$

with $\tilde{\gamma}^{\sigma c}$ refers as the ground-state spin σ 1RDM of the cluster obtained by solving \tilde{H}_{eff}^c defined in Equation (14).

In Figure 4, we show the representation of the projected hypersurface spanned by two variational parameters. It highlights the non-trivial shape of the landscape with local minima and flat zones. More precisely, we test the cost functions proposed in Equations (23), (25) and (27) with respect to two free parameters $\{\theta\}$ for $N_i = 1$, $N_b = 3$ and $r = 2$. A non-interacting one body reduced density matrix (idempotent) is used as a 1RDM test to obtain the transformation $\mathbf{R}^{\prime\sigma}(\theta)$. The first rank $r = 1$ vector is fixed using Block-Householder solution. The minimization of the buffer zone Δ (Figure 4a) strictly cancels the value of Δ and corresponds to the Block-Householder solution, as discussed in Section 2.1. This result is attributed to the fact that the trial density matrix is idempotent. However, this particular value is enclaved between regions of higher Δ values, which can make optimization difficult depending on the starting point of the numerical minimization. Subsequently, the minimization of the mean-field term between the cluster and the environment (Figure 4b) also yields the same solution in this case. However, the landscape is distinct from the previously studied cost function. Finally, the matching of the density matrices (Figure 4c) presents a very specific landscape. Indeed, such a landscape is numerically very challenging to explore in order to obtain the global minimum. Contrary to the cost functions studied previously, the Block-Householder solution (dark blue triangle) is not the global minimum. It appears that there exists a continuous set of minima, which further complicates the exploration of the landscape. Altogether, this highlights the non-trivial character of the resulting landscape that might display many local minima and quasi-flat

regions. As a result, the numerical optimization of the $\{\theta\}$ parameters might become challenging for a large number of parameters.

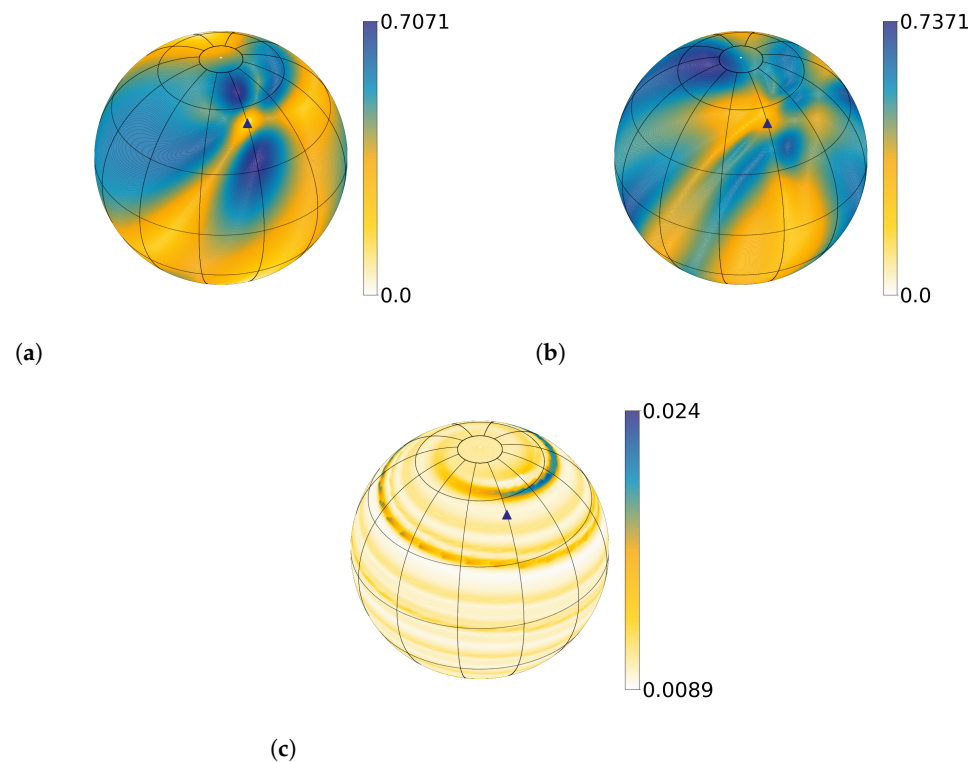


Figure 4. Evaluation of the cost functions with respect to free parameters $\{\theta\}$ for $N_i = 1$, $N_b = 3$ and $r = 2$ using a non-interacting one body reduced density matrix from a 1D Hubbard chain. The vector corresponding to the rank $r = 1$ is fixed and corresponds to the Block-Householder vector (see Figure 3), and the second is presented with the dark blue triangle. In this case, two angles are available, and are represented using spherical coordinates. The colorbar gives a continuous scale from the lowest value of the different cost function evaluation (white) to the highest (dark blue) for different cost functions. In (a), we evaluate the buffer-zone Δ (see Equation (23)). In (b), we evaluate the Hartree contribution E_H^2 (see Equation (25)) for $U/t = 8$, and in (c) we evaluate the density matrix matching (see Equation (27)) for $U/t = 8$.

3. Results and Discussion

In this section, the various cost functions outlined in Section 2.3 are evaluated against the homogeneous paramagnetic Hubbard model at half-filling, and compared to exact Bethe-Ansatz (BA) results [37,38], and against the standard Block-Householder transformation presented in Ref. [32] denoted by “BHt”. We recall that the BHt corresponds to a particular case, where the set of parameters $\{\theta\}$ is set according to the Equation (7). More specifically, the construction of the unitary transformation \mathbf{R}'^σ with the minimisation of the buffer in Equation (23) is denoted in the following with “Buffer”, the minimisation of the Hartree contribution of the interactions between the cluster and the environment in Equation (25) is denoted with “Hartree”, and by enforce the matching with density matrices with the Equation (27) with “Matching”. The non-idempotent N-representable 1RDM space is spanned using the self-consistent protocol presented in [32]. The various results pertain to the case of a single impurity. The generalization to multiple impurities, discussed in Section 2.2, will not be covered in this paper. For comparison purposes, the standard BHt method (gray lines) and the various cost function-based methods in this work (colored lines) are compared at the same level of numerical complexity, meaning that the clusters contain the same number of orbitals. For example, the single impurity and three orbitals in the bath in our approach are compared to the two impurities BHt, the latter containing two orbitals in the bath.

Additionally, the variational parameters are optimized using the numpy Python library [39], particularly with the L-BFGS-B method, which is similar to the conjugate gradient optimization method. Finally, as explained in [32], a damping parameter is added to avoid drastic changes in the 1RDM and convergence issues, meaning that a fraction of the previous 1RDM obtained is kept in the new 1RDM. In the results presented here, we used a damping of 60%.

In Figure 5, we show the relative error of the kinetic energy $\Delta E_k = 100 \times (E_K^{BA} - E_K) / E_K^{BA}$, where BA refers to the Bethe Ansatz solution, and the relative error of the double occupation $\Delta d = 100 \times (d^{BA} - d) / d^{BA}$ as a function of the relative correlation strength $U / (U + 4t)$, where $4t$ corresponds to the non-interacting band width. This figure presents the effect of the various cost functions outlined in Section 2.3 (color-coded lines). In this case, the single impurity $N_i = 1$ is embedded with three IB orbitals $N_b = 3$ for a vector \mathbf{V}' of rank $r = 2$. Thus, there is a number of parameters θ equal to $2 \times (3 - 1) = 4$ to optimize. In the non-interacting limit $U / (U + 4t) \rightarrow 0$, the kinetic energy and the double occupation are correctly reproduced for all cost functions. Regarding to the atomic limit $U / (U + 4t) \rightarrow 1$, the proposed modified embedding schemes are not suitable to recover the asymptotic behavior at this limit, as well as the BHT. For intermediate regimes $U / 4t \simeq 1$, there is a strong competition between electronic delocalization which increases kinetic energy, and the electron–electron repulsion strength which penalizes the number of double occupation. For state-of-the-art embedding methods, such as DMET [21] or the projected site-occupation embedding theory [18], describing this regime accurately is very challenging.

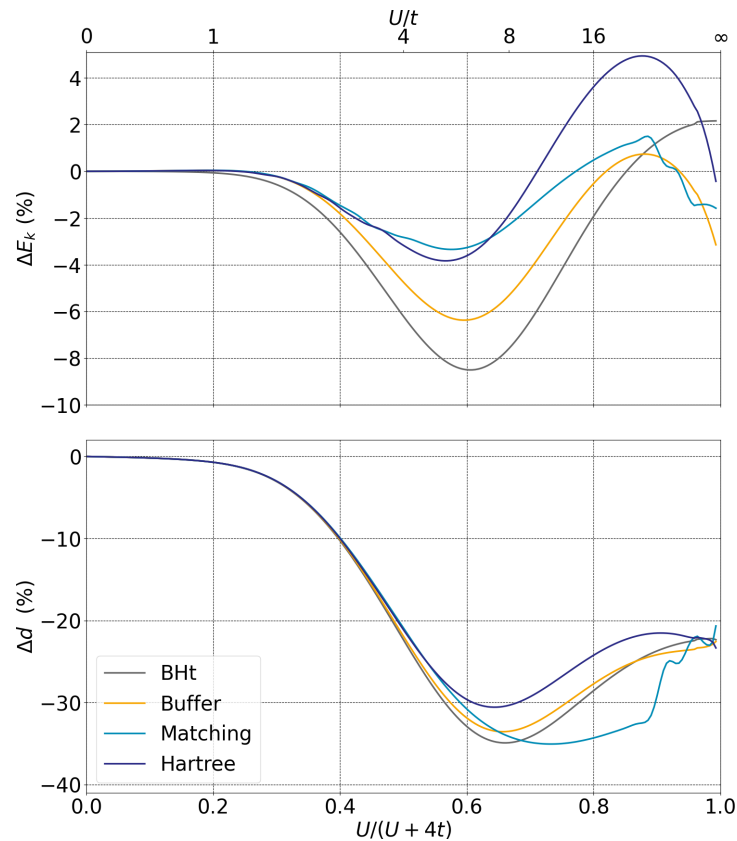


Figure 5. Relative error for the kinetic energy ΔE_k (**top** panel) and per site double occupation Δd (**bottom** panel) in percent with respect to correlation strength $U / (U + 4t)$ for one impurity orbital in the fragment, three bath orbitals and a rank two vector. Colored lines correspond to different cost functions.

For weakly-to-intermediate correlated regimes ($U / (U + 4t) < 0.6$), the results from the minimization of the cluster environment Hartree term (25) (dark blue line) are consistently better than those obtained by minimizing the buffer zone (23) (orange line), which

are in turn better than the Block-Householder solutions (gray line). However, the numerical cost associated with the minimization of constraint (25) scale as $\mathcal{O}(N_c N_e^4)$, which is significantly higher than the cost associated with constraint (23) scaling as $\mathcal{O}(N_c N_e^2)$, where N_e represents the number of orbitals belonging to the environment of the cluster, and N_c the number of orbitals belonging to the cluster. Concerning the one-body reduced density matrix matching proposed in Equation (27) (blue line), the results obtained are similar to the constraint (25) from low to middle correlated regime, and deviate for values of $U/(U + 4t) \simeq 0.6$ for kinetic energy and double occupancy. For strongly correlated regimes ($U/(U + 4t) \geq 0.6$), the interaction energy $E_{\text{int}} = U \times d$ dominates. Although the double occupancy is similar for the BHT and the buffer-zone minimization at this regime, the minimization of the mean-field term improves the results. The double occupancy is poorly described by the density matrix matching and exhibits nonphysical numerical instabilities for values of $U/(U + 4t) \rightarrow 1$.

In Figure 6, we show the evolution of the four different variational parameters θ for different cost functions as a function of relative correlation strength $U/(U + 4t)$ for a two rank r and a three bath orbitals calculation. In the left panel, we show the two variational parameters associated with rank $r = 1$, i.e., the first column of the matrix \mathbf{V}' in Equation (17), while in the right panel, the parameters are associated with rank $r = 2$. Solid lines correspond to the first angles for all ranks, and dotted lines to the second ones. Interestingly, we found that three among the four parameters do not change significantly with respect to $U/(U + 4t)$. While a definitive interpretation of this behavior remains challenging, it likely originates from system symmetries, specifically in this case, the translational and electron-hole symmetry, which significantly reduce and constrain the cost-function hyper-surface. Consequently, it is conceivable to simplify the variational optimization of the different parameters by considering only a reduced set of parameters (in this case the first of the second rank) varying significantly in the process. This simplification could greatly improve the numerical optimization of the parameters, and therefore the numerical efficiency of the method in general.

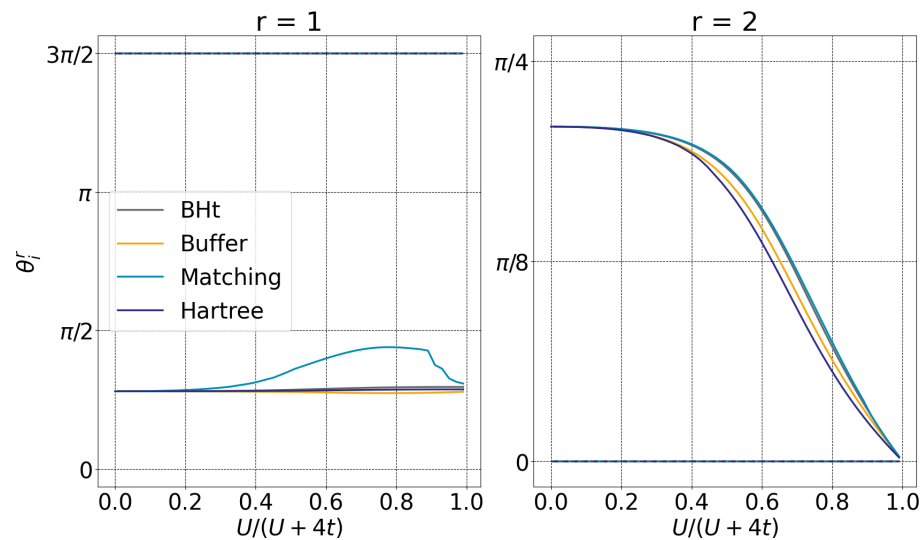


Figure 6. Optimized free-angle parameters with respect to the relative correlation strength $U/(U + 4t)$ for a rank $r = 2$ and a three bath orbitals calculation, for different cost functions (colored dashed lines). The left panel corresponds to the first rank, while the right panel to the second. Solid lines correspond to the first parameter of each rank, and dashed lines to the second.

As originally presented in DMET [21], the effective Hamiltonian was an AIM, which implies that interaction terms within the bath are neglected, a scenario referred to as the NIB approximation. In this context, we present in Figure 7 the relative error of the ground-state energy per site $E_{gs} = E_k + Ud$, with respect to the correlation strength for a system with a single impurity in the fragment, three bath orbitals, and a rank-two vector. In the low

correlation regime ($U/(U + 4t) < 0.3$), both NIB (represented by dashed colored lines) and IB (represented by full colored lines) yield similar results across all presented cost functions. However, for the intermediate to strong correlation regime ($U/(U + 4t) > 0.6$), the NIB approximation fails to provide an accurate description of the ground-state energy of the system. It should be noted that the BHt IB (full gray line) appears to offer the most accurate representation of the ground-state, contradicting the observations made in Figure 5. However, this apparent accuracy is misleading and arises from a larger error compensation between the kinetic and interaction energies. Additionally, we found the same error compensation for the NIB approximation, leading to inadequate results for both kinetic and interaction energies. It is also noteworthy to optimize variational parameters to minimize the strength of Coulomb repulsion in the bath. This method could potentially close the gap between finite interacting baths in DMET or DaC approaches, and the infinite but non-interacting baths present in DMFT.

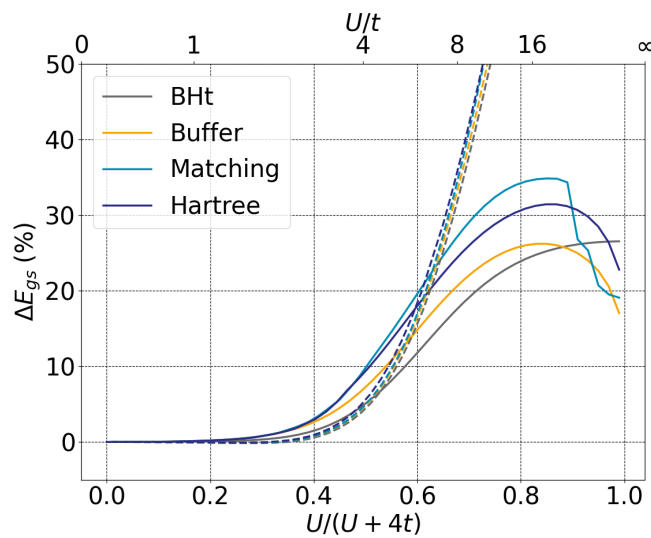


Figure 7. Relative error of the ground-state energy per site $\Delta E_{gs} = 100 \times (1 - E_{gs}/E_{BA})$ with respect to correlation strength $U/(U + 4t)$ for one impurity and three bath orbitals and a rank two vector. Colored lines correspond to different cost functions for the IB case, and dashed lines for the NIB case.

In the following, we focus on the IB case and the minimization of the buffer zone (see Equation (23)) to explore the influence of the number of bath orbitals and the rank of the matrix \mathbf{V}' used to define the unitary transformation. In Figure 8, we present the per site kinetic energy scaled with the non-interacting kinetic energy per site $E_K^0 = -4/\pi$ (upper panel) and the per site double occupation (lower panel) as a function of relative repulsion strength $U/(U + 4t)$. Results correspond to the cases $N_i = 1$, $N_b = 3$ and are given for different rank r of the vector \mathbf{V}' , ranging from one up to three. For instance, the rank two (orange line) corresponds to the results previously shown in Figure 5 (also with the orange line). The number of variational parameters is equal to 2 for $r = 1$, equal to 4 for $r = 2$, and equal to 6 for $r = 3$. For a rank 1 vector, we examine a special case where the rank equals the number of impurities N_i . In this case, the construction of vector \mathbf{V}' needs to satisfy only the norm preservation in Equation (21). As demonstrated previously in Section 2.2, increasing the rank of vector \mathbf{V}' does not systematically improve the solutions, as the accessible solution spaces are disjoint. Indeed, we show that the rank 2 results are the closest to the exact results for both kinetic energy and double occupation, and this applies to all correlation regimes $U/(U + 4t)$. For strongly correlated regimes, rank 3 slightly improves the results of rank 1, but exhibits numerical instabilities due to the optimization of a larger amount of variational parameters. According to this figure, it is not necessary to increase the rank of vector \mathbf{V}' in order to systematically improve the results. Moreover, the best results are obtained for $r = 2$, corresponding to the number of singular

values in DMET [21], or the number of columns of the vector $\mathbf{V}' = \mathbf{V}$ for the BHT presented here [32].

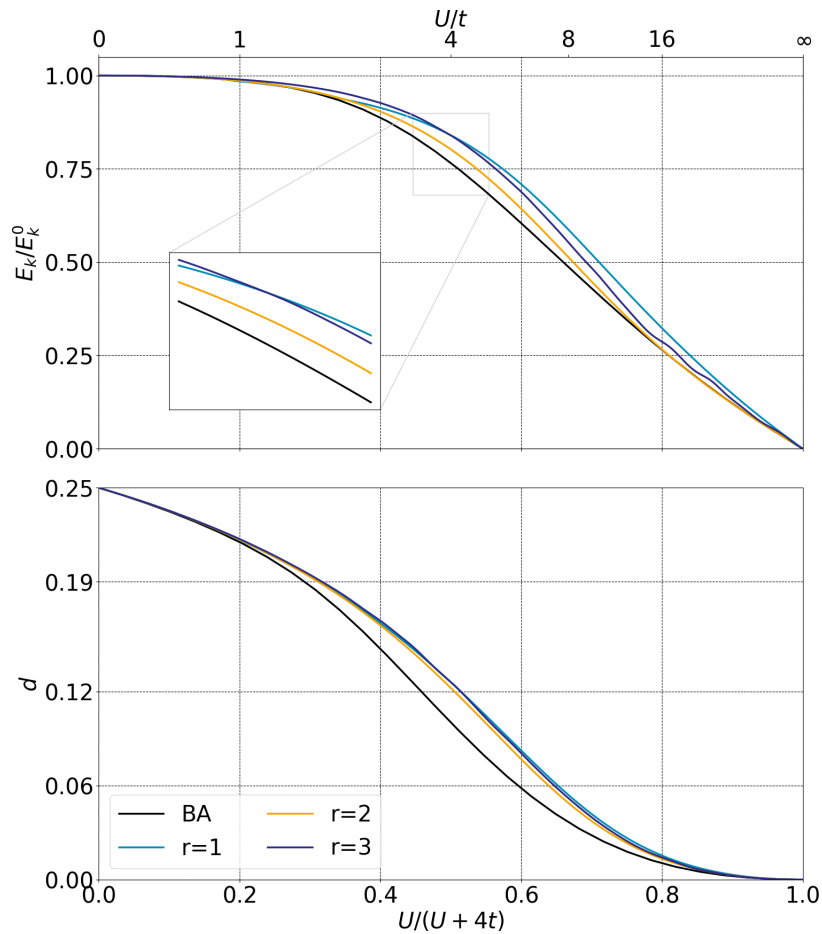


Figure 8. Renormalized kinetic energy per site E_k/E_k^0 (**top** panel) and per site double occupation d (**bottom** panel) with respect to correlation strength $U/(U + 4t)$ for one impurity and three bath orbitals and the minimization of the buffer zone as a cost function. Colored lines correspond to the rank of the vector up to three. Black solid line correspond to Bethe Ansatz.

In Figure 9, we present the scaled kinetic energy per site (upper panel) and the per site double occupation (lower panel) as a function of relative repulsion strength $U/(U + 4t)$. The results are shown for a rank $r = 3$ vector \mathbf{V}' , for different number of orbitals in the bath, ranging from one up to five (colored lines). For spin symmetry reasons, we only consider cases where the number of orbitals in the cluster is even. The case with a single orbital in the bath (yellow line) is very particular, as there are no variational parameters to be optimized in this case. In the other cases, the number of variational parameters corresponds to 6 for $N_b = 3$ orbitals (similarly as the orange line in Figure 5), and 12 for $N_b = 5$ orbitals. Importantly, increasing the number of orbitals in the bath systematically improves the kinetic energy and double occupation for all correlation regimes $U/(U + 4t)$. However, for strongly correlated regimes $U/(U + 4t) \gg 0.5$, we observe oscillations of the solutions for five bath orbitals likely due to the non-trivial and complex shape of the cost-function hyper-surface, which might be sharp and display many local minima at this limit.

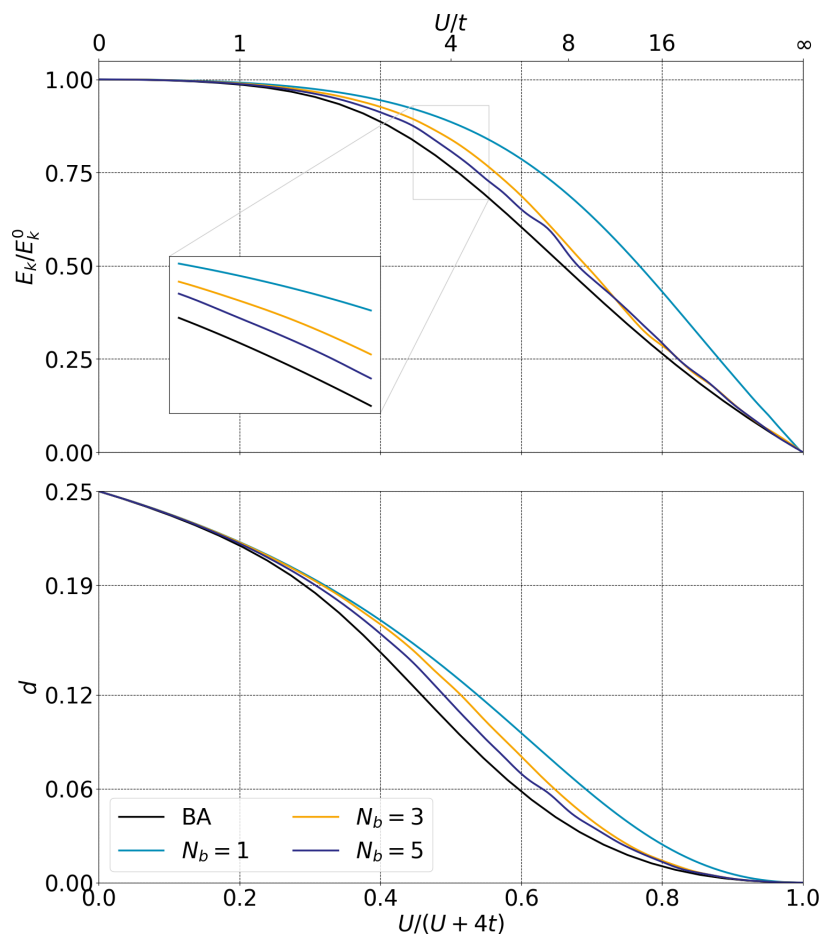


Figure 9. Renormalized kinetic energy per site E_k/E_k^0 (top panel) and per site double occupation d (bottom panel) with respect to correlation strength $U/(U + 4t)$ for a rank three vector and the minimization of the buffer zone as a cost function. Colored lines correspond to the number of bath orbitals up to five. Black solid line corresponds to Bethe Ansatz.

4. Conclusions

In this study, we have thoroughly investigated the performance of various 1RDM-based embedding methods to construct the orbitals of the bath. Particular emphasis is placed on the characteristics of the resulting reduced and effective Hamiltonian. Indeed, this Hamiltonian is tasked with accurately reproducing the interactions between the fragment of the system and its environment within a downscaled cluster.

While DMET employs the SVD of the fragment-environment 1RDM to define the effective Hamiltonian, we have demonstrated that the compact subspace is not the optimal setting for deriving the effective Hamiltonian. By generalizing the Block-Householder equations, we introduce a significant amount of additional flexible parameters, notably by adding bath orbitals that are nearly independent of the number of fragment orbitals or by exploring different transformation domains via rank augmentation. To efficiently leverage these additional degrees of freedom, we have proposed cost functions that, in most cases, effectively disconnect the cluster, containing an integer number of electrons, from the environment.

These cost functions were tested on the half-filled Hubbard model Hamiltonian, with a single impurity orbital in the fragment for which the equations are simplified. The results showed significant improvements over the Block-Householder outcomes.

Nevertheless, these improvements imply numerical optimization, which often proves challenging due to the complex landscape of cost functions. The complexity of these landscapes likely contributes to the fact that we can currently only achieve half-filled results. Moreover, this complexity occasionally makes it difficult to obtain continuous solutions for all relative correlation strengths, resulting in certain non-physical instabilities.

Therefore, we encourage further research into the development of efficient cost functions that can derive an optimized effective Hamiltonian to describe the fragment, offering a smoother landscape than its counterparts. A compelling challenge for future research would be to test the method on multiple impurity fragments and, importantly, to derive linearized equations to define the unitary transformation more effectively.

Author Contributions: Conceptualization, M.S. and Q.M.; methodology, M.S.; software, Q.M.; validation, M.S. and Q.M.; formal analysis, M.S. and Q.M.; investigation, M.S. and Q.M.; data curation, Q.M.; writing—original draft preparation, M.S. and Q.M.; writing—review and editing, M.S. and Q.M.; visualization, M.Q. and Q.M.; supervision, M.S.; project administration, M.S.; funding acquisition, M.S. All authors have read and agreed to the published version of the manuscript.

Funding: ANR (grant numbers: ANR-19CE29-0002 DESCARTES).

Institutional Review Board Statement: Not applicable.

Informed Consent Statement: Not applicable.

Data Availability Statement: Data are contained within the article.

Conflicts of Interest: The authors declare that they have no conflict of interest.

References

1. Sun, Q.; Chan, G.K.L. Quantum Embedding Theories. *Acc. Chem. Res.* **2016**, *49*, 2705–2712. [[CrossRef](#)]
2. Wasserman, A.; Pavanello, M. Quantum embedding electronic structure methods. *Int. J. Quantum Chem.* **2020**, *120*, e26495. [[CrossRef](#)]
3. Kotliar, G.; Savrasov, S.Y.; Pálsson, G.; Biroli, G. Cellular Dynamical Mean Field Approach to Strongly Correlated Systems. *Phys. Rev. Lett.* **2001**, *87*, 186401. [[CrossRef](#)]
4. Zheng, H. Self-consistent cluster-embedding calculation method and the calculated electronic structure of NiO. *Phys. Rev. B* **1993**, *48*, 14868–14883. [[CrossRef](#)] [[PubMed](#)]
5. Ma, H.; Sheng, N.; Govoni, M.; Galli, G. Quantum embedding theory for strongly correlated states in materials. *J. Chem. Theory Comput.* **2021**, *17*, 2116–2125. [[CrossRef](#)]
6. Cohen, A.J.; Mori-Sánchez, P.; Yang, W. Insights into Current Limitations of Density Functional Theory. *Science* **2008**, *321*, 792–794. [[CrossRef](#)]
7. Burke, K. Perspective on density functional theory. *J. Chem. Phys.* **2012**, *136*, 150901. [[CrossRef](#)]
8. Müller-Hartmann, E. Correlated fermions on a lattice in high dimensions. *Z. Für Phys. B Condens. Matter* **1989**, *74*, 507–512. [[CrossRef](#)]
9. Georges, A.; Kotliar, G.; Krauth, W.; Rozenberg, M.J. Dynamical mean-field theory of strongly correlated fermion systems and the limit of infinite dimensions. *Rev. Mod. Phys.* **1996**, *68*, 13–125. [[CrossRef](#)]
10. Georges, A.; Kotliar, G. Hubbard model in infinite dimensions. *Phys. Rev. B* **1992**, *45*, 6479–6483. [[CrossRef](#)]
11. Anderson, P.W. Localized magnetic states in metals. *Phys. Rev.* **1961**, *124*, 41. [[CrossRef](#)]
12. Potthoff, M. Self-energy-functional approach to systems of correlated electrons. *Eur. Phys. J. B* **2003**, *32*, 429–436. [[CrossRef](#)]
13. Sarker, S. A new functional integral formalism for strongly correlated fermi systems. *J. Phys. Condens. Matter* **1988**, *21*, L667. [[CrossRef](#)]
14. Mazouin, L.; Saubanère, M.; Fromager, E. Site-occupation Green's function embedding theory: A density functional approach to dynamical impurity solvers. *Phys. Rev. B* **2019**, *100*, 195104. [[CrossRef](#)]
15. Nguyen Lan, T.; Kananenka, A.A.; Zgid, D. Rigorous Ab Initio Quantum Embedding for Quantum Chemistry Using Green's Function Theory: Screened Interaction, Nonlocal Self-Energy Relaxation, Orbital Basis, and Chemical Accuracy. *J. Chem. Theory Comput.* **2016**, *12*, 4856–4870. [[CrossRef](#)]
16. Lupo, C.; Jamet, F.; Tse, T.; Rungger, I.; Weber, C. Maximally Localized Dynamical Quantum Embedding for Solving Many-Body Correlated Systems. *Nat. Comput. Sci.* **2021**, *1*, 410–420. [[CrossRef](#)]
17. Lanatà, N. Derivation of the Ghost Gutzwiller Approximation from Quantum Embedding principles: The Ghost Density Matrix Embedding Theory. *arXiv* **2023**, arXiv:2305.11895. [[CrossRef](#)]
18. Senjean, B. Projected site-occupation embedding theory. *Phys. Rev. B* **2019**, *100*, 035136. [[CrossRef](#)]
19. Sekaran, S.; Saubanère, M.; Fromager, E. Local potential functional embedding theory: A self-consistent flavor of density functional theory for lattices without density functionals. *Computation* **2022**, *10*, 45. [[CrossRef](#)]
20. Mitra, A.; Hermes, M.R.; Gagliardi, L. Density matrix embedding using multiconfiguration pair-density functional theory. *J. Chem. Theory Comput.* **2023**, *19*, 3498–3508. [[CrossRef](#)]
21. Knizia, G.; Chan, G.K.L. Density Matrix Embedding: A Simple Alternative to Dynamical Mean-Field Theory. *Phys. Rev. Lett.* **2012**, *109*, 186404. [[CrossRef](#)] [[PubMed](#)]

22. Wouters, S.; Jiménez-Hoyos, C.A.; Sun, Q.; Chan, G.K.L. A Practical Guide to Density Matrix Embedding Theory in Quantum Chemistry. *J. Chem. Theory Comput.* **2016**, *12*, 2706–2719. [[CrossRef](#)] [[PubMed](#)]
23. Yalouz, S.; Sekaran, S.; Fromager, E.; Saubanère, M. Quantum embedding of multi-orbital fragments using the block-Householder transformation. *J. Chem. Phys.* **2022**, *157*, 214112. [[CrossRef](#)] [[PubMed](#)]
24. Sekaran, S.; Bindech, O.; Fromager, E. A unified density matrix functional construction of quantum baths in density matrix embedding theory beyond the mean-field approximation. *J. Chem. Phys.* **2023**, *159*, 034107. [[CrossRef](#)]
25. Ayral, T.; Lee, T.H.; Kotliar, G. Dynamical mean-field theory, density-matrix embedding theory, and rotationally invariant slave bosons: A unified perspective. *Phys. Rev. B* **2017**, *96*, 235139. [[CrossRef](#)]
26. Cancès, E.; Faulstich, F.; Kirsch, A.; Letournel, E.; Levitt, A. Some mathematical insights on Density Matrix Embedding Theory. *arXiv* **2023**, arXiv:2305.16472. [[CrossRef](#)]
27. Sun, C.; Ray, U.; Cui, Z.H.; Stoudenmire, M.; Ferrero, M.; Chan, G.K.L. Finite-temperature density matrix embedding theory. *Phys. Rev. B* **2020**, *101*, 075131. [[CrossRef](#)]
28. Ye, H.Z.; Welborn, M.; Ricke, N.D.; Van Voorhis, T. Incremental embedding: A density matrix embedding scheme for molecules. *J. Chem. Phys.* **2018**, *149*, 194108. [[CrossRef](#)]
29. Hermes, M.R.; Gagliardi, L. Multiconfigurational Self-Consistent Field Theory with Density Matrix Embedding: The Localized Active Space Self-Consistent Field Method. *J. Chem. Theory Comput.* **2019**, *15*, 972–986. [[CrossRef](#)]
30. Sekaran, S.; Tsuchiizu, M.; Saubanère, M.; Fromager, E. Householder-transformed density matrix functional embedding theory. *Phys. Rev. B* **2021**, *104*, 035121. [[CrossRef](#)]
31. Hubbard, J. Electron correlations in narrow energy bands. *Proc. R. Soc. Lond. Ser. A* **1963**, *276*, 238–257. [[CrossRef](#)]
32. Marécat, Q.; Lasorne, B.; Fromager, E.; Saubanère, M. Unitary transformations within density matrix embedding approaches: A novel perspective on the self-consistent scheme for electronic structure calculation. *arXiv* **2023**, arXiv:2306.07641. <https://doi.org/10.48550/arXiv.2306.07641>.
33. Töws, W.; Pastor, G. Lattice density functional theory of the single-impurity Anderson model: Development and applications. *Phys. Rev. B* **2011**, *83*, 235101. [[CrossRef](#)]
34. Schade, R.; Blöchl, P.E. Adaptive cluster approximation for reduced density-matrix functional theory. *Phys. Rev. B* **2018**, *97*, 245131. [[CrossRef](#)]
35. Rotella, F.; Zambettakis, I. Block Householder transformation for parallel QR factorization. *Appl. Math. Lett.* **1999**, *12*, 29–34. [[CrossRef](#)]
36. Caffarel, M.; Krauth, W. Exact diagonalization approach to correlated fermions in infinite dimensions: Mott transition and superconductivity. *Phys. Rev. Lett.* **1994**, *72*, 1545–1548. [[CrossRef](#)]
37. Lieb, E.H.; Wu, F.Y. Absence of Mott Transition in an Exact Solution of the Short-Range, One-Band Model in One Dimension. *Phys. Rev. Lett.* **1968**, *20*, 1445–1448. [[CrossRef](#)]
38. Ogata, M.; Shiba, H. Bethe-ansatz wave function, momentum distribution, and spin correlation in the one-dimensional strongly correlated Hubbard model. *Phys. Rev. B* **1990**, *41*, 2326. [[CrossRef](#)]
39. Virtanen, P.; Gommers, R.; Oliphant, T.E.; Haberland, M.; Reddy, T.; Cournapeau, D.; Burovski, E.; Peterson, P.; Weckesser, W.; Bright, J.; et al. SciPy 1.0: Fundamental Algorithms for Scientific Computing in Python. *Nat. Methods* **2020**, *17*, 261–272. [[CrossRef](#)]

Disclaimer/Publisher’s Note: The statements, opinions and data contained in all publications are solely those of the individual author(s) and contributor(s) and not of MDPI and/or the editor(s). MDPI and/or the editor(s) disclaim responsibility for any injury to people or property resulting from any ideas, methods, instructions or products referred to in the content.